



HAL
open science

Velocity map imaging studies of the photodissociation of H_2O^+ cations.

Alan G Sage, Thomas A.A. Oliver, Richard N Dixon, Mike Ashfold

► **To cite this version:**

Alan G Sage, Thomas A.A. Oliver, Richard N Dixon, Mike Ashfold. Velocity map imaging studies of the photodissociation of H_2O^+ cations.. *Molecular Physics*, 2010, 108 (07-09), pp.945-955. 10.1080/00268971003596177 . hal-00596281

HAL Id: hal-00596281

<https://hal.science/hal-00596281>

Submitted on 27 May 2011

HAL is a multi-disciplinary open access archive for the deposit and dissemination of scientific research documents, whether they are published or not. The documents may come from teaching and research institutions in France or abroad, or from public or private research centers.

L'archive ouverte pluridisciplinaire **HAL**, est destinée au dépôt et à la diffusion de documents scientifiques de niveau recherche, publiés ou non, émanant des établissements d'enseignement et de recherche français ou étrangers, des laboratoires publics ou privés.



Velocity map imaging studies of the photodissociation of H₂O⁺ cations.

Journal:	<i>Molecular Physics</i>
Manuscript ID:	TMPH-2009-0359
Manuscript Type:	Special Issue Paper - In honour of Prof Richard Zare
Date Submitted by the Author:	09-Nov-2009
Complete List of Authors:	Sage, Alan; University of Bristol, Chemistry Oliver, Thomas; University of Bristol, Chemistry Dixon, Richard; University of Bristol, Chemistry Ashfold, Mike; Bristol University
Keywords:	photodissociation, H ₂ O cations, velocity map imaging, multiphoton ionization
Note: The following files were submitted by the author for peer review, but cannot be converted to PDF. You must view these files (e.g. movies) online.	
submitted material.zip	



Velocity map imaging studies of the photodissociation of H₂O⁺ cations.

Alan G. Sage, Thomas A.A. Oliver, Richard N. Dixon and Michael N.R. Ashfold

School of Chemistry, University of Bristol, Bristol BS8 1TS, U.K.

Figures: 5

Author for correspondence:

Prof. M.N.R. Ashfold

(address as above)

Tel: +44 (0)117 928 8312

Fax: +44 (0)117 925 0612

e-mail: mike.ashfold@bris.ac.uk

Abstract

The near-threshold photofragmentation dynamics of state-selected H_2O^+ cations have been investigated using velocity map ion imaging methods. The cations were prepared in the $v=0$ level of the ground ($\tilde{X}^2\text{B}_1$) electronic state, by 2+1 resonance enhanced multiphoton ionization via selected rotational levels of the H_2O , $\tilde{C}^1\text{B}_1$, $v=0$ state. Subsequent two photon excitation of the resulting H_2O^+ cations to $\tilde{B}^2\text{B}_2$ state levels lying above the lowest dissociation limit (*i.e.* at total energies in the range 46000 - 50600 cm^{-1}) results in O–H bond fission and OH^+ fragment ion formation. These fragments display isotropic recoil velocity distributions, which peak at low kinetic energy but extend to the highest speeds allowed by energy conservation. *Ab initio* calculations of key sections through the potential energy surfaces (PESs) for the ground and first few excited states of H_2O^+ suggest two possible mechanisms for the observed rotational and (when energetically allowed) vibrational excitation of the OH^+ fragments. Both require initial non-adiabatic (vibronic coupling) from the photo-prepared \tilde{B} state level to high levels of the $\tilde{A}^2\text{A}_1$ state, but involve different subsequent $\text{HO}^+\text{--H}$ bond fission mechanisms. One involves Renner-Teller coupling to the ground state PES, while the alternative requires spin-orbit induced coupling to the repulsive $\tilde{a}^4\text{B}_1(4\text{A}'')$ state PES.

1. Introduction

Detailed investigations of the photodissociation dynamics of gas phase molecular cations are becoming increasingly commonplace [1-15]. Typically, these studies employ resonance enhanced multiphoton ionisation (REMPI) to prepare the cations with a high degree of internal (vibrational and rotational) quantum state selectivity. Velocity mapped ion imaging methods [16,17] are very well suited to such experiments, since subsequent photolysis of the cation necessarily results in formation of a charged photo-product, the recoil velocity (speed and angular) distributions of which are revealed in the image without the need for further experimental influence. The literature contains numerous reports describing aspects of the photochemistry of neutral water molecules [18-20], but quantitative photochemical data relating to its cation is much less common – notwithstanding the importance of chemistry involving H_2O^+ cations in the upper atmosphere [21], in comet tails [22] and in interstellar clouds [23]. Here we describe one approach that goes some way towards rectifying this deficiency.

H_2O has the electronic configuration $(1a_1)^2(2a_1)^2(1b_2)^2(3a_1)^2(1b_1)^2$. The ground, first and second excited states of H_2O^+ are of particular relevance in the present work. Within the framework of molecular orbital (MO) theory, these can be described in terms of electron removal from, respectively, the $1b_1$, $3a_1$ and $1b_2$ orbital, yielding the \tilde{X}^2B_1 , \tilde{A}^2A_1 and \tilde{B}^2B_2 states. These three states have very different equilibrium geometries [24]. Ground state H_2O^+ is formed by removing an electron from the O-centred $1b_1$ ‘lone pair’ orbital (that lies orthogonal to the molecular plane), giving a state of 2B_1 symmetry with a bent geometry – similar to that of neutral H_2O . This bent geometry can be understood in terms of the competing forces arising from electrons in the $3a_1$ and $1b_2$ orbitals. The $1b_1$ and $3a_1$ orbitals are degenerate at linear geometries, but the latter is stabilised by progressive acquisition of s character upon bending. Removal of a $3a_1$ electron reduces this bending force, and the \tilde{A}^2A_1 state has a quasi-linear equilibrium geometry. In contrast, the \tilde{B}^2B_2 state (formed by removing a $1b_2$ electron) is very bent, with an acute equilibrium bond angle. The \tilde{A}^2A_1 and \tilde{X}^2B_1 states are the two halves of a degenerate ($^2\Pi$) state at linear geometries and, as such, constitute a text-book example of a Renner-Teller coupled system [25,26].

1
2
3
4 The photoelectron spectrum of H₂O is consistent with the foregoing MO description, displaying
5 discrete bands associated with ionization to the \tilde{X}^2B_1 , \tilde{A}^2A_1 and \tilde{B}^2B_2 states of the cation [27-
6 30]. The first photoelectron band is dominated by the origin transition, but also shows weak
7 activity in both ν_1 (the symmetric stretching mode) and ν_2 (the bend) – consistent with minimal
8 change in equilibrium geometry upon removing a $1b_1$ electron. The second photoelectron band
9 shows an extensive series of peaks, which have been assigned to progressions in ν_2 built on 0
10 and 1 quanta of ν_1 – consistent with the large increase in equilibrium bond angle in the \tilde{A}^2A_1
11 state (relative to the ground state neutral). High resolution photoelectron spectroscopy reveals
12 additional fine structure within these peaks, attributable to vibronic (Renner-Teller) coupling
13 with levels of the \tilde{X} state. The third photoelectron band (associated with formation of \tilde{B}^2B_2
14 state ions) displays extensive structure also. This structure is much more diffuse, however, and
15 has thus far defied consistent assignment – even when recorded using a rotationally cold sample
16 [29]. The diffuse nature of this band is attributable to predissociation of the \tilde{B}^2B_2 state [31,32].
17 Photoelectron-photoion coincidence studies of both H₂O and D₂O show that O–H/D bond
18 fission and formation of ground ($X^3\Sigma^-$) state OH⁺/OD⁺ fragments together with H/D atoms is the
19 sole fragmentation pathway at threshold, but identify an increasing role for the alternative
20 products (OH/OD($X^2\Pi$) + H⁺/D⁺) as the excitation energy is increased. ‘Symmetric’
21 dissociation to O⁺ products is also possible within the energy range investigated in this work,
22 but is found to have negligible quantum yield [33-35]. These behaviours have been discussed
23 within the framework of the then available PESs for the electronic states of interest [32,36]. As
24 shown in greater detail later, the \tilde{B}^2B_2 ($^2A'$ in C_s) state potential correlates diabatically with the
25 high energy H + OH⁺($a^1\Delta$) asymptote upon O–H bond extension, but is crossed by potentials
26 associated with the a^4B_1 ($^4A''$) and \tilde{A}^2A_1 ($^2A'$) states. Spin-orbit induced predissociation by the
27 former, and/or vibronic coupling to the latter (mediated by ν_3 , the asymmetric stretching mode)
28 and subsequent non-adiabatic coupling to the $^4A''$ PES, have both been proposed as routes to the
29 observed OH⁺ and H⁺ products following excitation to the \tilde{B}^2B_2 state [32,35].
30
31
32
33
34
35
36
37
38
39
40
41
42
43
44
45
46
47
48
49
50
51
52

53 MPI spectra of H₂O and D₂O, resonance enhanced at the energies of both three and two
54 absorbed photons (*i.e.* 3+1 and 2+1 REMPI spectra) reveal a wealth of rovibronic structure
55 associated with Rydberg states belonging to series that converge to the first ionization limit [37-
56 39]. More recent 2+1 REMPI-photoelectron spectroscopy studies served to demonstrate a
57 strong propensity for Franck-Condon diagonal ($\Delta v = 0$) ionization from these Rydberg states
58
59
60

[40,41]. Of particular relevance to the present work, 2+1 REMPI via the $\tilde{C}^1B_1, v=0$ level was shown to yield H_2O^+/D_2O^+ ions exclusively in the lowest (zero-point) vibrational level.

The $\tilde{A}-\tilde{X}$ systems of H_2O^+ and D_2O^+ have been studied in absorption [42] and in emission from electric discharges [43,44]. These spectra exhibit rich rotational structure superimposed on a progression in v_2 . The ground states of H_2O and H_2O^+ have very similar equilibrium geometries. Analogy with the first photoelectron band suggests that the $H_2O^+(\tilde{A}-\tilde{X})$ progression exhibits peak intensity at $v_2' \sim 7-8$, but $H_2O^+(\tilde{A})$ state levels with $v_2' \leq 15$ (and energies $\sim 23300 \text{ cm}^{-1}$) have been identified in the emission spectrum. The $\tilde{B}^2B_2-\tilde{X}^2B_1$ transition is electric dipole forbidden, but allowed in two photon excitation. For future reference, we can use (at least) two different thermodynamic cycles to establish the threshold energies for forming $H+OH^+(X^3\Sigma^-)$ and $H^+ + OH(X^2\Pi)$ products from the ground state of $H_2O^+(\tilde{X}^2B_1)$ cations. The more direct cycle starts from the appearance energy for forming OH^+ fragment ions in the photoionization of H_2O , $AE(OH^+/H_2O) = 146117 \pm 24 \text{ cm}^{-1}$ [45] which, when combined with the best available value of the ionisation potential of H_2O ($101766 \pm 2 \text{ cm}^{-1}$ [46]), yields $D_0(H-OH^+) = 44351 \pm 26 \text{ cm}^{-1}$. Given the ionisation potentials of the OH radical ($104989 \pm 2 \text{ cm}^{-1}$ [47]) and the H atom (109677 cm^{-1} [48]), the threshold energy for proton formation follows as $D_0(H^+-OH) = 49039 \pm 26 \text{ cm}^{-1}$. The alternative route to these quantities starts with the most direct measure of $D_0(H-OH)$, $41151 \pm 5 \text{ cm}^{-1}$ [49], which, when combined with the ionization potentials of H_2O , OH and H yields $D_0(H-OH^+) = 44374 \pm 9 \text{ cm}^{-1}$ and $D_0(H^+-OH) = 49062 \pm 9 \text{ cm}^{-1}$.

The present imaging study employs 2+1 REMPI at selected wavelengths λ_1 (and wavenumbers $\tilde{\nu}_1$) chosen to be resonant with different rotational levels of the $\tilde{C}^1B_1, v=0$ state to prepare $H_2O^+(\tilde{X}^2B_1, v=0)$ cations. The $H_2O^+(\tilde{B}-\tilde{X})$ transition is electric dipole forbidden. Thus we employ a two-photon scheme, exciting these cations at wavelength λ_2 (wavenumber $\tilde{\nu}_2$), selected to be resonant at the one photon energy with one or more rovibronic levels of the \tilde{A} state. This results in population of the \tilde{B}^2B_2 state at total (two photon) wavenumbers in the range $46000 \leq 2\tilde{\nu}_2 \leq 50600 \text{ cm}^{-1}$, above the first dissociation threshold – thereby allowing exploration of the fragmentation dynamics of these excited cations to $H + OH^+$ products. This experimental program is complemented by new *ab initio* calculations of key sections of the

1
2
3 potential energy surfaces (PESs) of the ground and first five excited electronic states of H_2O^+ ,
4 which also serve to aid our understanding of this fragmentation process. Finally, we report the
5 observation of an additional velocity component evident within the OH^+ images recorded at
6 certain specific $\tilde{\nu}_2'$ wavenumbers (where the requisite $\tilde{\nu}_2'$ is produced by frequency doubling
7 radiation of wavenumber $\tilde{\nu}_2$). This additional component is attributed to unintended three
8 photon ionisation of highly rotationally excited $\text{OH}(\text{X})$ fragments. These are deduced to be
9 formed by predissociation from the $\tilde{\text{C}}^1\text{B}_1, v=0$ state, with the subsequent ionisation process
10 resonance enhanced at the two photon energy by an, as yet unidentified, Rydberg state of OH .
11
12
13
14
15
16
17
18
19
20

2. Experimental

21
22
23 The ion imaging apparatus was used without significant modification from previous studies
24 [11,50]. Deionised water was placed in a gas bulb and thoroughly degassed by exposure to
25 vacuum. The bulb was then filled with 200-400 mbar argon gas, and allowed to equilibrate with
26 the room temperature vapour pressure of the water. This in turn was passed through an in-line
27 filter containing glass wool soaked in further degassed, deionised water and resistively heated to
28 $\sim 60^\circ\text{C}$, increasing the partial pressure of water vapour. The gas mixture was expanded through
29 a pulsed valve, forming a molecular beam, which was directed through a skimmer into the
30 source region of a differentially pumped imaging spectrometer. The outputs of two Nd:YAG
31 pumped dye lasers (often after frequency doubling) were counter-propagated through the
32 interaction region, at 90° to the molecular beam axis, and focussed ($f = 20$ cm lens) so as to
33 overlap the latter spatially (in the interaction region) but with a temporal separation $\delta t \sim 30$ ns –
34 thereby ensuring multiphoton excitation and ionization of the neutral H_2O molecules prior to
35 photolysis of the resulting cations. Typical pulse energies were: $E_1 \leq 2.5$ mJ pulse $^{-1}$ after
36 frequency doubling the fundamental dye laser output to generate $\lambda_1 \sim 248$ nm; $E_2 \leq 15$ mJ pulse $^{-1}$
37 when λ_2 was a fundamental dye laser wavelength (*i.e.* $\lambda_2 > 400$ nm), but ≤ 2 mJ pulse $^{-1}$ in the case
38 of frequency doubled radiation ($\lambda_2' < 300$ nm). The polarisation vectors of both laser beams, $\boldsymbol{\varepsilon}_1$
39 and $\boldsymbol{\varepsilon}_2$, were arranged to be vertical in the lab. frame (*i.e.* to be aligned parallel to the front face
40 of the detector). Ions formed in the interaction region were accelerated under velocity mapping
41 conditions towards a time and position sensitive detector – a pair of microchannel plates (MCPs)
42 coupled to a fast phosphor screen positioned 860 mm beyond the interaction region. $\sim 10\%$ of
43 the resulting emission was separated using a quartz beamsplitter and directed to a
44 photomultiplier to obtain time-of-flight (TOF) spectra of the ions formed in the interaction
45
46
47
48
49
50
51
52
53
54
55
56
57
58
59
60

1
2
3
4
5
6
7
8
9
10
11
12
13
14
15
16
17
18
19
20
21
22
23
24
25
26
27
28
29
30
31
32
33
34
35
36
37
38
39
40
41
42
43
44
45
46
47
48
49
50
51
52
53
54
55
56
57
58
59
60

volume. The remainder was read by a CCD camera (Photonic Science) equipped with a fast intensifier gated to the TOF of the OH^+ fragments of interest. The image resulting from each laser shot was processed with an event counting, centroiding algorithm provided with the commercial software DaVis (LaVision) and the resulting counts summed for, typically, 2×10^4 laser shots. Analysis of the accumulated ion images involved reconstruction of the 3-D recoil velocity distribution as described previously [50] using an algorithm based on the filtered back-projection method of Sato *et al* [51]. 2-D slices through these reconstructed images were converted to total kinetic energy release (TKER) data using eq. (1)

$$\text{TKER} = \frac{1}{2} m_{\text{OH}^+} \left(1 + \frac{m_{\text{OH}^+}}{m_{\text{H}}} \right) v_{\text{OH}^+}^2, \quad (1)$$

and the resulting intensities scaled with the appropriate Jacobian. Photofragment excitation (PHOFEX) spectra for forming OH^+ ions following preparation of the state-selected parent cation were recorded also, by measuring the intensity of the m/z 17 peak in the TOF spectrum as a function of $\tilde{\nu}_2$ wavenumber – which was calibrated by directing a portion of the dye laser output into a wavemeter (Coherent Wavemaster).

3. Electronic structure calculations

Multi-reference Configuration Interaction with Davidson correction (MRCI+Q) calculations were performed in MOLPRO2006 [52], using a 7/9 CI space, freezing only the $1s$ oxygen orbital. To achieve the correct Rydberg mixing, the basis set was an admixture of Dunning's basis functions; for oxygen, d -aug-cc-pVTZ was used and supplemented with extra s and p functionals and d and f functionals from aug-cc-pVTZ; for hydrogen, only the cc-pVTZ basis was required. The minimum energy geometry of the ground state was found to be $\angle\text{HOH} = 102.5^\circ$ and $R_{\text{O-H}} = 1.03 \text{ \AA}$. For dissociation in C_s symmetries, $\angle\text{HOH}$ was fixed to 102.5° and one $R_{\text{O-H}}$ varied. For the bending potentials, $\angle\text{HOH}$ was varied and both $R_{\text{O-H}}$ fixed to 1.03 \AA ; calculations were also performed varying $\angle\text{HOH}$ and fixing both $R_{\text{O-H}}$ at 1.5 \AA .

4. Results

4.1 Imaging the process $\text{H}_2\text{O}^+ + 2h\nu_2 \rightarrow \text{H} + \text{OH}^+$

TOF mass spectra obtained following excitation at $\tilde{\nu}_1$ wavenumbers that match with documented 2+1 REMPI transitions of H_2O show a large peak at m/z 18 (associated with parent H_2O^+ ions) and a small OH^+ signal. Introducing suitably delayed $\tilde{\nu}_2$ photons of appropriate wavenumber results in a significant increase in the m/z 17 peak intensity.

Figure 1 shows PHOFEX spectra obtained by monitoring the OH^+ ion yield as a function of $\tilde{\nu}_2$, following parent ion preparation by 2+1 REMPI via (a) the $2_{20}-1_{01}$ line ($2\tilde{\nu}_1 = 80725.2 \text{ cm}^{-1}$), (b) the blended $3_{22}-3_{03}$ and $3_{13}-2_{12}$ lines ($2\tilde{\nu}_1 = 80674.1 \text{ cm}^{-1}$) and (c) the $1_{11}-1_{10}$ line ($2\tilde{\nu}_1 = 80616.5 \text{ cm}^{-1}$) of the $\tilde{\text{C}}-\tilde{\text{X}}$ (0,0) transition. Each shows fine structure that, on energetic grounds, we associate with transitions within the $\tilde{\text{A}}-\tilde{\text{X}}$ (0,14,0-0,0,0) band, and an underlying background signal (from unintended but unavoidable fragment ion formation by λ_1 photons). Given the limited available spectroscopic data for this $\tilde{\text{A}}-\tilde{\text{X}}$ band, and uncertainties regarding the particular rotational levels of $\text{H}_2\text{O}^+(\tilde{\text{X}})$ populated at the different REMPI wavelengths, we have not attempted detailed assignment of the structure in these spectra. The dashed line at $\tilde{\nu}_2 = 22187 \text{ cm}^{-1}$ indicates the energetic threshold for forming $\text{H} + \text{OH}^+$ fragments by two photon photolysis of $\text{H}_2\text{O}^+(\tilde{\text{X}}, v=0, N=0)$ parent ions; reassuringly, most of the structured OH^+ yield appears at higher wavenumber. These are some of the most intense two colour PHOFEX spectra obtained, reflecting the strength of the respective 2+1 REMPI transitions, and the extent of resonance enhancement provided by $\text{H}_2\text{O}^+(\tilde{\text{A}}-\tilde{\text{X}})$ transitions at wavenumber $\tilde{\nu}_2$ to energies above the dissociation threshold. Two colour PHOFEX spectra recorded at higher $\tilde{\nu}_2$ showed poorer signal to noise ratios on account of the decreasing $\tilde{\text{A}}-\tilde{\text{X}}$ and/or $\tilde{\text{B}}-\tilde{\text{A}}$ Franck-Condon factors.

OH^+ ion images were recorded following excitation on various of the stronger resonances in the range spanned by fig. 1 and at many higher $\tilde{\nu}_2$ wavenumbers. Figure 2 shows a representative set of images, and $\text{H} + \text{OH}^+$ TKER distributions derived there from using eq. (1). Parent ion preparation in each case employed the $\tilde{\text{C}}-\tilde{\text{X}}$, (0,0), $2_{20}-1_{01}$ line (which typically gave the largest parent H_2O^+ ion signal), but the measured images were not obviously sensitive to the particular choice of REMPI transition. The α value required for converting the radii of the measured images into the corresponding OH^+ fragment speeds, and thence the TKER, was obtained by measuring $^{35}\text{Cl}^+$ fragment ion images from the well characterised photodissociation

of DCI^+ parent ions [7] using the same velocity mapping conditions. The combs festooned above the intensity versus TKER plots show TKER values predicted for the different $\text{H} + \text{OH}^+$ product channels assuming dissociation via



and use of the energy conserving relation eq. (3):

$$\text{TKER} = 2h\nu_2 + E_{\text{int}}(\text{H}_2\text{O}^+) - D_0(\text{H}-\text{OH}^+) - E_{\text{int}}(\text{OH}^+(\text{X}, v, N)). \quad (3)$$

$E_{\text{int}}(\text{OH}^+(\text{X}, v, N))$, the rovibrational term values of the possible OH^+ product states, were calculated using the spectral simulation package PGOPHER [53] and spectroscopic constants for the $\text{OH}^+(\text{X}^3\Sigma^-)$ cation taken from the literature [54]. As discussed earlier, we take $D_0(\text{H}-\text{OH}^+) = 44374 \text{ cm}^{-1}$ and, in the absence of better information, take the mean internal energy of the parent cation to be equal to that of the 2_{20} level of the $\tilde{\text{C}}^1\text{B}_1, v=0$ state that provides the resonance enhancement when preparing the parent ions for these imaging studies (*i.e.* $E_{\text{int}}(\text{H}_2\text{O}^+) \sim 124 \text{ cm}^{-1}$). In reality, one photon ionization from the $\tilde{\text{C}}, v=0, J_{KaKc}=2_{20}$ level is likely to result in population of several N_{KaKc} rotational levels of the cation, with different $E_{\text{int}}(\text{H}_2\text{O}^+)$ values and different two photon dissociation probabilities at any given $\tilde{\nu}_2$ wavenumber. This constitutes one factor limiting the energy resolution of the present experiments but, as in most cation fragmentation experiments, space charge effects will generally be the most important factor limiting the achievable energy resolution. Such Coulombic interactions will be particularly burdensome in the present case, since we not only create comparatively high densities of parent H_2O^+ cations in a localised volume, but then choose to monitor the comparatively heavy, and thus slowly recoiling, fragment ion (OH^+).

OH^+ ion images recorded at $2\tilde{\nu}_2$ wavenumbers close above the dissociation (*e.g.* at $\tilde{\nu}_2 = 22405 \text{ cm}^{-1}$, fig. 2(a)) show a small, unresolved central feature attributable to the dissociation process (2). Energy conservation dictates that the $\text{OH}^+(\text{X})$ fragments are formed in their $v=0$ state and in low N rotational levels. A second ring associated with faster OH^+ products is clearly evident in all of these images, and in the corresponding intensity versus TKER plots. The radius of this feature is too large to be associated with the intended dissociation (2), and appears unchanged when the λ_2 photons are blocked. This is the signature of unwanted OH^+ fragments formed by λ_1 photons only; the one colour image shows this ‘fast’ ring, and variable amounts of signal at very low TKER. The energy of a single $\tilde{\nu}_1$ photon is insufficient to excite $\text{H}_2\text{O}^+(\tilde{X}, v=0)$

1
2
3
4
5
6
7
8
9
10
11
12
13
14
15
16
17
18
19
20
21
22
23
24
25
26
27
28
29
30
31
32
33
34
35
36
37
38
39
40
41
42
43
44
45
46
47
48
49
50
51
52
53
54
55
56
57
58
59
60

cations above the threshold for dissociation process (2). Thus the most likely explanation for the broad distribution of $\text{H} + \text{OH}^+$ fragments arising via one ($\tilde{\nu}_1$) colour excitation, centred at $\text{TKER} \sim 4000 \text{ cm}^{-1}$, is dissociative ionization following absorption of four $\tilde{\nu}_1$ photons by neutral H_2O molecules. Note that the maximum possible TKER for $\text{H} + \text{OH}^+$ products arising via such a three body dissociative ionization process (*i.e.* in the case that the departing photoelectron takes none of the excess energy) would be $\sim 15000 \text{ cm}^{-1}$.

As fig. 2 shows, the distribution of OH^+ internal energies expands and shows a clear preference for populating higher N rotational levels upon tuning to higher $\tilde{\nu}_2$ wavenumbers. Peaks associated with population of individual high N levels are discernable at the low energy end of the intensity versus TKER plots shown in figs. 2(c) and 2(d), but the images show no recoil anisotropy. The relative importance of the low TKER feature grows as $\tilde{\nu}_2$ is increased further. This feature could be associated with population of yet higher N levels of $\text{OH}^+(\text{X}, v=0)$, but the energy spacing between such high rotational levels should be resolvable with the present imaging apparatus. Population of $\text{OH}^+(\text{X}, v=1)$ product states is thus a more likely assignment for this slow feature – as illustrated in figs. 2(e) and 2(f). Unfortunately, it is not possible to deconvolute the relative contributions that $\text{OH}^+ v=0$ and $v=1$ products make to this feature. The measured OH^+ signal intensities decrease with increasing $\tilde{\nu}_2$ (as reflected by the poorer quality of the images displayed in figs. 2(e) and (f)), to the point that we were unable to acquire images at $\tilde{\nu}_2 > 25333 \text{ cm}^{-1}$ – presumably because of declining Franck-Condon factors for the $\tilde{\text{A}} - \tilde{\text{X}}$ and/or $\tilde{\text{B}} - \tilde{\text{A}}$ excitation steps.

OH^+ ion images were also measured using single UV photons, at a number of $\tilde{\nu}_2'$ wavenumbers that were roughly twice those used when imaging the two photon dissociation products shown in fig. 2. The UV ($\tilde{\nu}_2'$) pulse energies were $\sim 10\%$ those available from the dye laser fundamental output (at wavenumber $\tilde{\nu}_2$), and any ‘two colour’ OH^+ signal was hard to discern over the unintended one ($\tilde{\nu}_1$) colour signal. Such a finding is consistent with the fact that the $\text{H}_2\text{O}^+(\tilde{\text{B}} - \tilde{\text{X}})$ transition should be one photon forbidden, by symmetry. OH^+ ion images recorded at $\tilde{\nu}_2' = 48014 \text{ cm}^{-1}$, however, showed an additional feature: a narrow, anisotropic ring centred at $\text{TKER} \sim 17100 \text{ cm}^{-1}$. Discussion of this feature is reserved until section 4.3.

In summary, two photon dissociation of $\text{H}_2\text{O}^+(\tilde{\text{X}}, v=0)$ cations at energies close above the threshold for process (2) results in formation of $\text{OH}^+(\text{X})$ fragments with substantial rotational

(and, when energetically possible, vibrational) excitation – a finding that broadly parallels the conclusions reached in earlier dissociative photoionization studies of $D_2O^+(\tilde{B}^2B_2)$ cations and which encouraged the suggestion that complex non-adiabatic dynamics were involved in the dissociation process [35].

4.2 Potential energy surfaces for the ground and first few excited states of H_2O^+

Dynamical interpretation is aided by the selected cuts through the PESs for the \tilde{X} , \tilde{A} , \tilde{B} and \tilde{a}^4B_1 states of H_2O^+ shown in fig. 3. The right hand panel illustrates how the potential energies of these states varies with extension of one O–H bond, while maintaining the other OH bond length and the inter-bond angle at their ground state equilibrium values (calculated as $R_{O-H} = 1.03 \text{ \AA}$ and $\angle HOH = 102.5^\circ$ (*cf* experimental values of 1.00 \AA and $\angle HOH = 109.3^\circ$ [55], and previous computational values of 0.96 \AA and 102.5° [56])). The ground (\tilde{X}^2B_1) and repulsive (\tilde{a}^4B_1) states – both of A'' symmetry once the cation is distorted away from C_{2v} geometries – correlate to the $H+OH^+(X^3\Sigma^-)$ limit, while the potentials of the first excited \tilde{A}^2A_1 state ($^2A'$ in C_s) and of a dissociative 2B_1 state ($^2A''$ in C_s) correlate to the limit $H^+ + OH(X^2\Pi)$. The left hand panel displays two sets of cuts through the various PESs. The solid curves show how the PE varies with $\angle HOH$ while maintaining C_{2v} symmetry and the two OH bond lengths $R_{O-H(1)}$ and $R_{O-H(2)}$ fixed at the ground state equilibrium value. The dashed curves show the corresponding potentials when $R_{O-H(1)} = 1.03 \text{ \AA}$ but $R_{O-H(2)} = 1.50 \text{ \AA}$ (*i.e. en route* to $H+OH^+$ (or $H + OH^+$), products). These calculations succeed in reproducing the ground state equilibrium bond angle, capture the degeneracy of the \tilde{X} and \tilde{A} states at linear geometries, and highlight the small equilibrium bond angle of the \tilde{B}^2B_1 state ($\angle HOH \sim 54^\circ$) and the CI between the \tilde{B} and \tilde{A} state PESs – which have the same (A') symmetry upon extending one O–H bond. They also show that the minimum energy geometry of the \tilde{a}^4B_1 state ($^4A''$ in C_s) is linear and that, in contrast to the three bound states, its PE decreases upon extension of one O–H bond. The angular anisotropy of the \tilde{a}^4B_1 state PES also decreases upon extending $R_{O-H(2)}$.

Armed with these PESs, we see that the present two photon absorption by $H_2O^+(\tilde{X}, v=0)$ cations involves double resonant excitation, via high v_2 bending levels of the \tilde{A}^2A_1 state, to the \tilde{B}^2B_1 state. The topology of the \tilde{B} state PES will encourage a reduction in $\angle HOH$ (and some (symmetric) increase in $R_{O-H(1)}$ and $R_{O-H(2)}$ [56]), steering the excited cations towards the CI

linking the \tilde{B} and \tilde{A} state PESs and promoting non-adiabatic transfer to the latter PES. As fig. 3 shows, the topology of the \tilde{A} state PES will encourage increasing $\angle\text{HOH}$ and large amplitude bending motion. As noted previously, the \tilde{A} state PES correlates with $\text{H}^+\text{OH}(\text{X})$ products, and the earlier dissociative photoionization studies showed this channel increasing in relative importance with increasing photon energy [35]. This fragmentation pathway is not accessible at the excitation energies used in the present study however. As fig. 3 also shows, there are two non-adiabatic routes by which $\text{H}_2\text{O}^+(\tilde{A})$ molecules can dissociate to ground state $\text{H} + \text{OH}^+$ products, both of which are favoured by linear (or near-linear) geometries. One involves spin-orbit coupling to the $\tilde{a}^4\text{B}_1(4\text{A}'')$ PES. The other recognises that the \tilde{A} and \tilde{X} states are a Renner-Teller pair and degenerate at linear geometries, and that a -axis rotation (Coriolis coupling) will facilitate $\tilde{A} \rightsquigarrow \tilde{X}$ transfer when $\angle\text{HOH} \sim 180^\circ$. Both mechanisms might be expected to give rise to qualitatively similar energy disposals in the eventual $\text{OH}^+(\text{X})$ products: rotation by virtue of the large amplitude bending vibration activated by $\tilde{B} \leftarrow \tilde{A} \leftarrow \tilde{X}$ excitation and the subsequent $\tilde{B} \rightsquigarrow \tilde{A} \rightsquigarrow \tilde{X} / \tilde{a}$ non-adiabatic transfers; and vibration, either as a result of parent stretching motion initiated on the \tilde{B} state PES or, feasibly, by coupling with large amplitude bending motion on the \tilde{A} and/or \tilde{X} PESs. Unfortunately the present data, taken with a higher level of initial state preparation and with higher product kinetic energy resolution than any reported hitherto, is still unable to provide a definitive distinction between these two possible non-adiabatic pathways.

4.3 Imaging the process $\text{H}_2\text{O} + 2h\nu_1 \rightarrow \text{H} + \text{OH}(\text{X})$

Figures 4(a) – 4(c) show further two colour OH^+ ion images. These were recorded using $\tilde{\nu}_1 = 40249.7 \text{ cm}^{-1}$, 40362.6 cm^{-1} and 40337.3 cm^{-1} , respectively, with, in each case, $\tilde{\nu}_2' = 48014 \text{ cm}^{-1}$ and delayed by $\delta t \sim 30 \text{ ns}$. Two photon excitation at these $\tilde{\nu}_1$ wavenumbers excites, respectively, the $0_{00}-2_{21}$ line, the $2_{20}-1_{01}$ line and the blended $3_{13}-2_{12}$ and $3_{22}-3_{03}$ lines of the $\tilde{C}-\tilde{X}$ (0,0) band. The cores of these two colour images, and of those recorded when exciting several other neighbouring two photon resonances, are very similar to those of the one colour images recorded at the corresponding $\tilde{\nu}_1$ wavenumbers. The feature of particular interest in these images is the anisotropic annular ring at much larger radius, however. As the partner intensity versus TKER plot (fig. 4(d)) shows, this feature has an associated $\langle\text{TKER}\rangle \sim 17100 \text{ cm}^{-1}$. This is a sharp resonance, the observation of which requires $\tilde{\nu}_2'$ to be set at this precise

wavenumber; tuning $\tilde{\nu}_2'$ by $\pm 1 \text{ cm}^{-1}$ suffices to cause the fast ring to disappear. Figures 4(e) – 4(g) show the way in which the fast OH^+ ion signal varies as a function of θ (defined relative to $\boldsymbol{\varepsilon}_1$ and $\boldsymbol{\varepsilon}_2$, which are both vertical in the plane of the displayed image). These clearly vary with $\tilde{\nu}_1$, *i.e.* with the particular choice of $\tilde{\text{C}}-\tilde{\text{X}}$ (0,0) resonance. The smooth curve through each data set is the line of best fit using eq. (4)

$$P(\theta) = \frac{1}{4\pi} \left[1 + \sum_{n=2,4} \beta_n P_n(\cos\theta) \right], \quad (4)$$

where the β_n are anisotropy parameters and P_n are n^{th} order Legendre polynomials. The best-fit β_n values returned by fitting the angular distributions in figs. 4(e)–4(g) vary markedly. The first and last are dominated by the P_2 term ($\beta_2 = -0.43 \pm 0.01$, $\beta_4 = -0.01 \pm 0.01$, and $\beta_2 = -0.28 \pm 0.01$, $\beta_4 = 0.09 \pm 0.01$, respectively), whereas the angular anisotropy of the image shown in fig. 4(b) is dominated by the P_4 term ($\beta_2 = -0.06 \pm 0.01$, $\beta_4 = -0.32 \pm 0.02$).

Figure 5 summarises the energetics of OH^+ cation formation from resonance enhanced two photon dissociation of H_2O^+ cations with $\tilde{\nu}_2$ photons, as described in sections 4.1 and 4.2. Such a process, labelled (1) in fig. 5, is incapable of generating $\text{H} + \text{OH}^+$ fragments with sufficient TKER to account for the observed fast two colour signal, or of displaying such sensitivity to the precise value of $\tilde{\nu}_2$. Similar arguments lead us to discount $\text{H}_2\text{O}^+(\tilde{\text{B}} \leftarrow \tilde{\text{X}})$ excitation by absorption of a single $\tilde{\nu}_2'$ photon as a possible source of the fast OH^+ fragments; such a scenario is rendered even less likely by the dipole forbidden nature of the $\text{H}_2\text{O}^+(\tilde{\text{B}} \leftarrow \tilde{\text{X}})$ transition. Figure 5 also indicates an alternative route to OH^+ cation formation, however, that is consistent with the present observations. This alternative route, process (2), is enabled by predissociation of $\text{H}_2\text{O}(\tilde{\text{C}})$ molecules following absorption of two $\tilde{\nu}_1$ photons. Yuan *et al.* [57] have reported H (Rydberg) atom photofragment translational spectroscopy studies of rovibrationally state-selected $\text{H}_2\text{O}(\tilde{\text{C}})$ state molecules following one (vacuum UV) photon excitation; the resulting OH fragments are formed in both their $\text{X}^2\Pi$ and $\text{A}^2\Sigma^+$ states, and in a broad spread of internal energy states. Given $D_0(\text{H}-\text{OH}) = 41151 \pm 5 \text{ cm}^{-1}$ [49], the determined TKER $\sim 17100 \text{ cm}^{-1}$ implies that the radical fragment is formed with $E_{\text{int}} \sim 22470 \text{ cm}^{-1}$, which matches well with the term value of the $\text{OH}(\text{X}, v=0, N=37)$ level [58]. Such highly rotationally excited, vibrationally cold $\text{OH}(\text{X})$ fragments are characteristic of photo-excited $\text{H}_2\text{O}(\tilde{\text{C}})$ molecules that dissociate by Coriolis coupling to the $\tilde{\text{B}}^1\text{A}_1$ state and subsequent non-adiabatic

coupling via the CI linking the \tilde{B} and \tilde{X} state PESs [49,59]. Ionisation of an OH(X) fragment requires the absorption of a minimum of three $\tilde{\nu}_2'$ photons, and the extreme sensitivity to the choice of $\tilde{\nu}_2'$ suggests that this three photon ionisation is strongly resonance enhanced. Given that there are no real excited states of OH at the one photon energy [60], we conclude that the resonance enhancing state lies at the energy of two $\tilde{\nu}_2'$ photons (*i.e.* at $\sim 96028 \text{ cm}^{-1}$). This is higher in energy than any currently documented 2+1 REMPI transition of the OH radical [61]. It is not possible at this time to establish either the symmetry of the resonance enhancing state, or the rotational branch by which it is being reached, but it is likely to be a Rydberg state with vibrational and rotational constants comparable to (but somewhat smaller than) those of the ground electronic state. As such, we can anticipate that the 2+1 REMPI spectrum will exhibit open rotational structure, especially at high N – consistent with the present identification of just one (high N) transition in the narrow $\tilde{\nu}_2'$ wavenumber range investigated.

Qualitatively, at least, the recoil anisotropy of these fast OH⁺ fragments is also consistent with the above mechanism. As discussed elsewhere (in the context of one photon induced dissociation of H₂O(\tilde{C}) molecules [57]), there is a clear distinction between the (relatively long) rotational timescale of the quasi-bound excited state molecule and the eventual (fast) O–H bond fission. The observed recoil anisotropy of the H and OH fragments can then be represented as a mapping of the distribution of recoil paths in the body-fixed frame (α, β) onto the anisotropic distribution of the quasi-bound excited molecules in the space fixed frame (θ, ϕ). The latter varies between the rotational levels and excitation branches [62]. Of particular relevance to the present data:

$$\beta_2(\text{H, OH}) = \sum_m A_{2m} \times a_{2m} \quad m = -2, 0, 2 \quad (5a)$$

$$\beta_4(\text{H, OH}) = \sum_m A_{4m} \times a_{4m} \quad m = -4, -2, 0, 2, 4 \quad (5b)$$

The spatial alignment factors, A_{nm} , can be calculated using rotational angular momentum expectation values, whereas the a_{nm} are moments in an associated Legendre basis $P_n^m(\alpha\beta)$ of the recoil in the body-fixed axis system. If the REMPI transition used to detect the OH(X, $v=0$, $N=37$) fragments was saturated, then the recoil anisotropy of the OH⁺ product would relate directly to that given by eq. (5). In general, however, the REMPI detection step will also have an intrinsic anisotropy [63], and the observed OH⁺ product recoil anisotropy will be the convolution of these two separate steps.

We have evaluated the A_{nm} factors for the relevant transitions, and sought a set of a_{nm} values with which to reconcile the observed β_2 and β_4 values, but without success. We note in this respect that excitation through the \tilde{C} , $v=0$, 0_{00} level (fig. 4(a)) – which must result in an isotropic ensemble of OH radicals – nonetheless leads to an anisotropic OH⁺ product recoil. This must stem from the REMPI detection step and, by inference, apply to the distributions measured when exciting the other parent levels. Unfortunately there are too many unknowns regarding the body-fixed dissociation moments and the states involved in the REMPI detection step for us to be able to provide a consistent and unambiguous interpretation of the limited experimental data. That said, it is clear that the variation of the observed OH⁺ recoil anisotropy must derive from the varying magnitudes and signs of the A_{nm} factors from one transition to another.

5. Discussion

The primary focus of this study is to provide improved insight into the near threshold fragmentation dynamics of H₂O⁺ cations, and the summary discussion that follows centres on this topic. First, it is instructive to compare and contrast the present findings with those of the heavier homologue, H₂S⁺. The PESs for the ground and first few excited states of these two cations show many qualitative similarities, but one key difference is the relative energetic ordering of the various dissociation thresholds. The lowest energy dissociation limit in H₂S⁺ is the symmetric elimination channel forming S⁺(⁴S) fragment ions along with H₂ molecules – which is observed to be open at, or just above, the energetic threshold ($\tilde{\nu}_2 \sim 23769$ cm⁻¹, $\lambda_2 \sim 421$ nm). One photon excitation to energies just above this threshold promotes H₂S⁺ cations to high bending vibrational levels of the \tilde{A}^2A_1 state, which are deduced to evolve (via Renner-Teller coupling) to high vibrational levels of the ground (\tilde{X}) state, at near linear configurations, and thence (by spin-orbit coupling) to the dissociative ⁴A₂ PES and eventual S⁺ + H₂ products. Imaging studies succeeded in demonstrating the rigorous mapping of the nuclear spin (ortho-/para-) parity of the initial H₂S molecule through to the eventual H₂ products [11,12]. Studies of the rotational energy disposal within the H₂ products as a function of λ_2 identified the onset of an alternative route to these same products at wavelengths below ~ 335 nm, wherein the photo-excited H₂S⁺(\tilde{A}) cations access the dissociative ⁴A₂ PES by non-adiabatic coupling through the alternative \tilde{B}^2B_1 state. The alternative fragmentation process, yielding H + SH⁺(X³Σ⁻)

1
2
3
4 products, is only open, energetically, once $\lambda_2 < 325$ nm [64]. Imaging studies of the resulting
5 SH^+ products imply a propensity for channelling excess energy over and above that required for
6 bond fission into product rotation [12]. Again, it is possible to visualise (at least) two routes to
7 forming these products following initial excitation of high vibrational levels of the $\tilde{\text{A}}^2\text{A}_1$ state:
8 vibronic mixing with levels of the $\tilde{\text{B}}^2\text{B}_2$ state, followed by spin-orbit induced transfer to the
9 lowest $^4\text{A}''$ PES [65-67] and/or non-adiabatic (Renner-Teller) coupling to the ground state PES
10 [12] – both of which lead, asymptotically, to HS^+-H bond fission.
11
12
13
14
15
16
17

18 In contrast to H_2S^+ , the lowest energy fragmentation pathway in H_2O^+ involves O–H bond
19 fission rather than H_2 elimination. The latter channel reportedly has negligible quantum yield in
20 the wavelength range of present interest [33-35]. Since $D_0(\text{HO}^+-\text{H})$ is almost twice the
21 magnitude of $D_0(\text{HS}^+-\text{H})$, studies of the near threshold photofragmentation of H_2O^+ cations
22 require use of substantially larger (UV) photon energies or, as here, the use of two visible ($\tilde{\nu}_2$)
23 photons. The lowest dissociation threshold corresponds to energies within the $\tilde{\text{B}}$ state
24 manifold. $\tilde{\text{B}}^2\text{B}_2-\tilde{\text{X}}^2\text{B}_1$ excitation involves an electronic transition moment of A_2 symmetry
25 and, as such, is electric dipole forbidden but allowed in two photon excitation. The resulting
26 near threshold dissociation, which shows clear evidence of resonance enhancement at the energy
27 of one absorbed photon by high vibrational levels of the $\tilde{\text{A}}^2\text{A}_1$ state, yields $\text{H} + \text{OH}^+(\text{X}^3\Sigma^-)$
28 fragments with increasing amounts of rotational and (when energetically possible) vibrational
29 excitation in the radical product as λ_2 is reduced.
30
31
32
33
34
35
36
37
38
39
40
41

42 The measured product energy disposal is consistent with a dissociation mechanism whereby the
43 initially prepared $\text{H}_2\text{O}^+(\tilde{\text{B}})$ cations decay by non-adiabatic (vibronic) coupling to high levels of
44 the $\tilde{\text{A}}^2\text{A}_1$ state and subsequent HO^+-H bond fission following (Renner-Teller) coupling to the
45 ground state PES and/or (spin-orbit induced) coupling to the $\tilde{\text{a}}^4\text{A}''$ state PES. The latter
46 possibility is of particular note. The dominant electronic configuration associated with the
47 repulsive $\tilde{\text{a}}^4\text{A}''$ state is derived by promoting an electron from the doubly occupied $3a_1$ MO to
48 the lowest unoccupied ($4a_1$) MO. As fig. 3(a) shows, the minimum energy geometry of this
49 state is linear, at all $R_{\text{O-H}}$. The $4a_1$ orbital involves substantial 3s Rydberg character in the
50 vertical Franck-Condon region, but progressively acquires σ^* anti-bonding character (localised
51 on the dissociating bond) as $R_{\text{O-H}}$ is increased. In this regard, the $\tilde{\text{a}}^4\text{A}''$ state of the H_2O^+ cation
52 has some parallels with the (better studied) $\tilde{\text{B}}^1\text{A}_1$ state of neutral H_2O . The two states share a
53
54
55
56
57
58
59
60

1
2
3
4 common set of occupied bonding and anti-bonding valence electrons, differing only in the
5 number of non-bonding $1b_1$ electrons. Thus the forces acting on the nuclei as they evolve on
6 both PESs are likely to encourage similar motions – *i.e.* simultaneous opening of $\angle\text{HOH}$ and
7 extension of $R_{\text{O-H}}$ – and rotationally excited diatomic fragments should be expected (and are
8 indeed observed). The literature contains many examples of photo-excited neutral molecules
9 that dissociate by bond fission on excited $\pi\sigma^*$ (or $n\sigma^*$) PESs [68]. One signature of such
10 dissociations is a markedly non-statistical energy disposal in the products (*e.g.* predominant
11 channelling of the excess energy into product translation, or product rotation). The presence of
12 low lying excited valence states in most open shell species (*e.g.* the $\tilde{\text{A}}$ and $\tilde{\text{B}}$ states in the case
13 of H_2O^+) ensures that there are, as yet, few recognised examples of the involvement of such
14 repulsive excited states in the fragmentation of molecular cations, but the eventual dissociation
15 of H_2O^+ cations on the $\tilde{\text{a}}^4\text{A}''$ state PES appears to constitute one such example.
16
17
18
19
20
21
22
23
24
25
26

27 **Acknowledgements**

28 The authors are grateful to the EPSRC and the EU for financial support through, respectively, a
29 programme grant (EP/G00224X) and a Marie Curie Initial Training Network (ICONIC, contract
30 agreement no. 238671), and to A.D. Webb, B.B. Seebohm, J.N. Harvey, K.N. Rosser and J.A.
31 Smith for their many and varied contributions to the work described in this paper.
32
33
34
35
36
37
38
39
40
41
42
43
44
45
46
47
48
49
50
51
52
53
54
55
56
57
58
59
60

Figure Captions

Figure 1

PHOFEX spectra obtained by monitoring the OH^+ ion yield in the range $22150 \leq \tilde{\nu}_2 \leq 22500$ cm^{-1} following preparation of H_2O^+ parent ions by 2+1 REMPI via (a) the $2_{20}-1_{01}$ line ($2\tilde{\nu}_1 = 80725.2$ cm^{-1}), (b) the blended $3_{22}-3_{03}$ and $3_{13}-2_{12}$ lines ($2\tilde{\nu}_1 = 80674.1$ cm^{-1}) and (c) the $1_{11}-1_{10}$ line ($2\tilde{\nu}_1 = 80616.5$ cm^{-1}) of the $\tilde{\text{C}}-\tilde{\text{X}}$ (0,0) two photon transition. The dashed line at $\tilde{\nu}_2 = 22187$ cm^{-1} indicates the energetic threshold for forming OH^+ ions by two photon excitation of $\text{H}_2\text{O}^+(\tilde{\text{X}}, v=0, N=0)$ parent ions.

Figure 2

OH^+ ion images, and the associated $\text{H} + \text{OH}^+$ TKER distributions derived there from, obtained following preparation of $\text{H}_2\text{O}^+(\tilde{\text{X}}, v=0)$ cations by 2+1 REMPI via the $\tilde{\text{C}}, v=0, J_{KaKc} = 2_{20}$ level ($\tilde{\nu}_1 = 40362.6$ cm^{-1}) and subsequent two photon dissociation at $\tilde{\nu}_2 =$ (a) 22405 cm^{-1} , (b) 23159 cm^{-1} , (c) 23351 cm^{-1} , (d) 23360 cm^{-1} , (e) 24302 cm^{-1} and (f) 25333 cm^{-1} . The polarisation vectors of both laser beams, $\boldsymbol{\epsilon}_1$ and $\boldsymbol{\epsilon}_2$, were aligned vertically in the plane of the page.

Figure 3

Cuts through the PESs for the $\tilde{\text{X}}^2\text{B}_1$, $\tilde{\text{A}}^2\text{A}_1$, $\tilde{\text{B}}^2\text{B}_2$ and $\tilde{\text{a}}^4\text{B}_1$ states of H_2O^+ , and for a higher repulsive $^2\text{B}_1$ state correlating to the $\text{H}^+ + \text{OH}$ limit, calculated at the MRCI+Q/(7/9)/ aug-cc-pVTZ level, freezing only the $1s$ oxygen orbital as described in the text: (a) bending potentials, varying $\angle\text{HOH}$ while (i) maintaining the O–H bond lengths at $R_{\text{O-H}(1)} = R_{\text{O-H}(2)} = 1.03$ \AA (solid curves), and (ii) extending $R_{\text{O-H}(2)}$ to 1.5 \AA while holding $R_{\text{O-H}(1)} = 1.03$ \AA (dashed curves); (b) dissociation coordinate varying $R_{\text{O-H}(2)}$ while maintaining $\angle\text{HOH}$ and $R_{\text{O-H}(1)}$ at the calculated ground state equilibrium values (102.5° and 1.03 \AA , respectively).

Figure 4

OH^+ ion images recorded following excitation at $\tilde{\nu}_1 =$ (a) 40249.7 cm^{-1} , (b) 40362.6 cm^{-1} and (c) 40337.3 cm^{-1} , with $\tilde{\nu}_2' = 48014$ cm^{-1} , a time delay $\delta t \sim 30$ ns and both $\boldsymbol{\epsilon}_1$ and $\boldsymbol{\epsilon}_2$ aligned vertically in the plane of the page. (d) Intensity versus TKER plot derived from image (b). Panels (e) – (g) show plots of signal intensity versus angle θ derived from images (a) – (c). The smooth curve through each of these data sets is the line of best fit using eq. (4) with (e) $\beta_2 =$

1
2
3
4 -0.43 ± 0.01 , $\beta_4 = -0.01 \pm 0.01$, (f) $\beta_2 = -0.06 \pm 0.01$, $\beta_4 = -0.32 \pm 0.02$, (g) $\beta_2 = -0.28 \pm 0.01$, $\beta_4 =$
5 0.09 ± 0.01 .
6
7

8 9 **Figure 5**

10 Summary overview of the mechanisms and energetics of OH^+ cation formation by (1) resonance
11 enhanced two ($\tilde{\nu}_2$) photon photolysis of H_2O^+ cations as described in sections 4.1 and 4.2 and
12 (2) 2+1 REMPI (at wavenumber $\tilde{\nu}_2'$) of OH fragments resulting from predissociation of
13 $\text{H}_2\text{O}(\tilde{\text{C}}^1\text{B}_1)$ molecules as described in section 4.3.
14
15
16
17
18
19
20
21
22
23
24
25
26
27
28
29
30
31
32
33
34
35
36
37
38
39
40
41
42
43
44
45
46
47
48
49
50
51
52
53
54
55
56
57
58
59
60

Figure 1

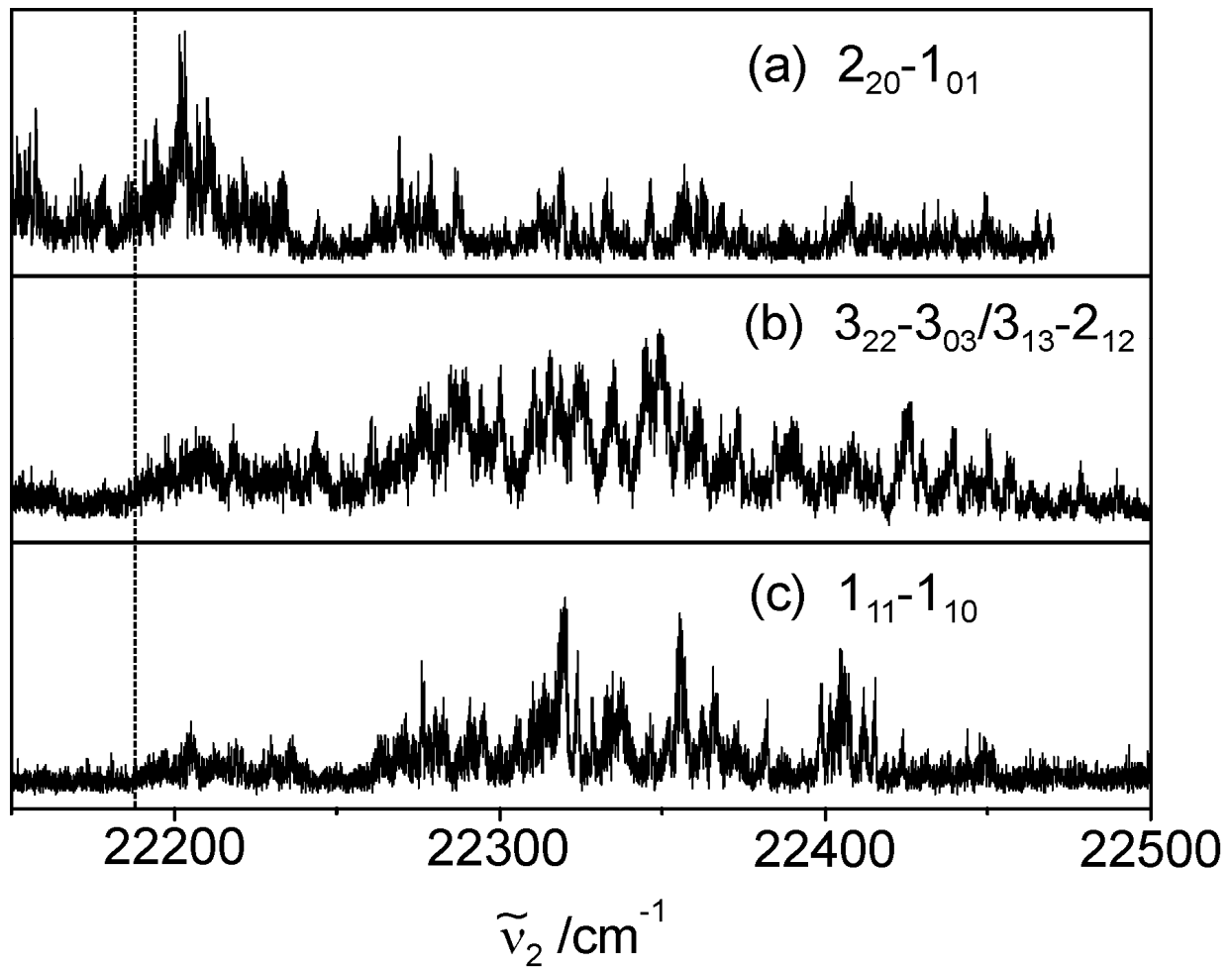


Figure 2

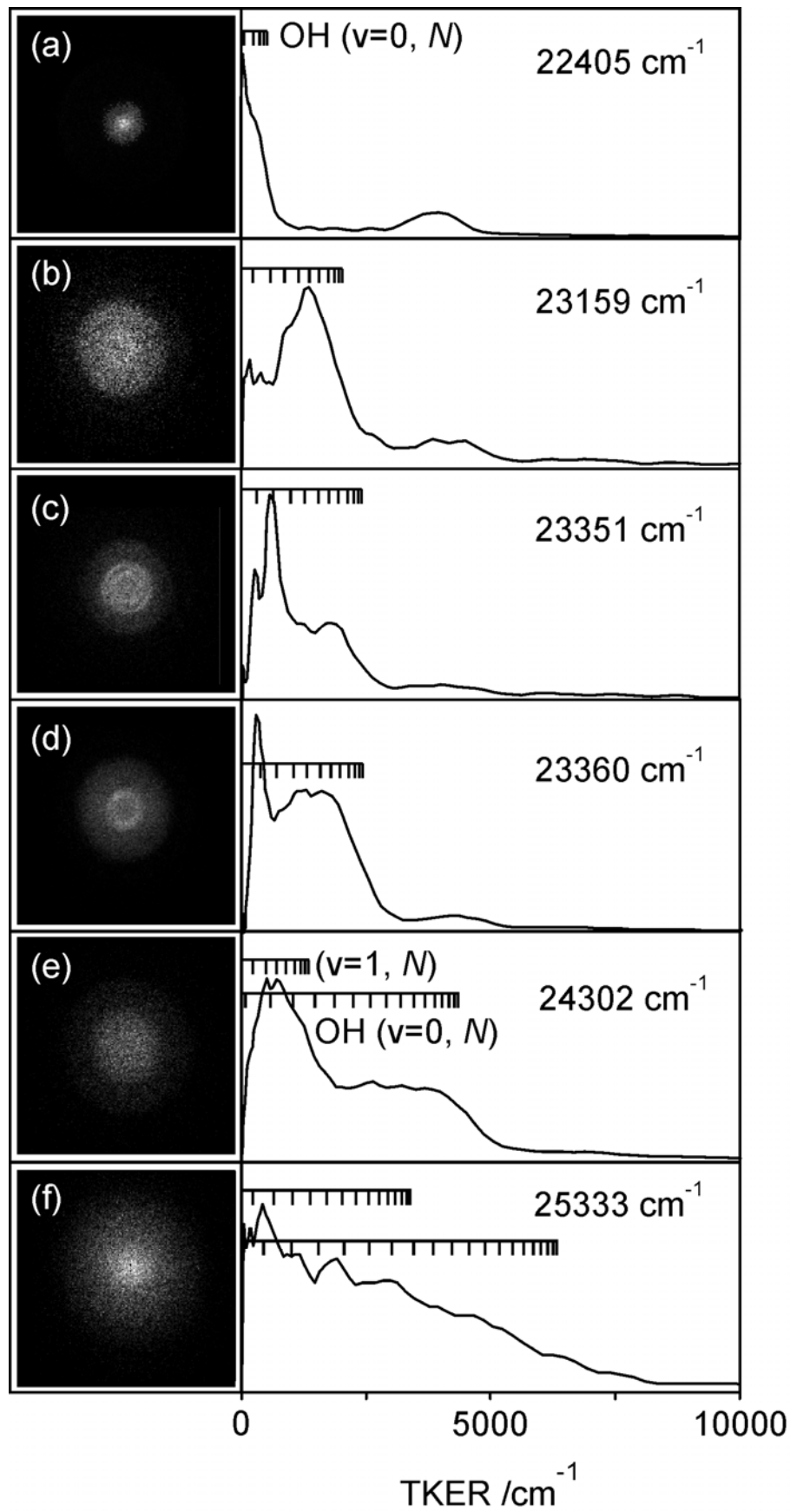
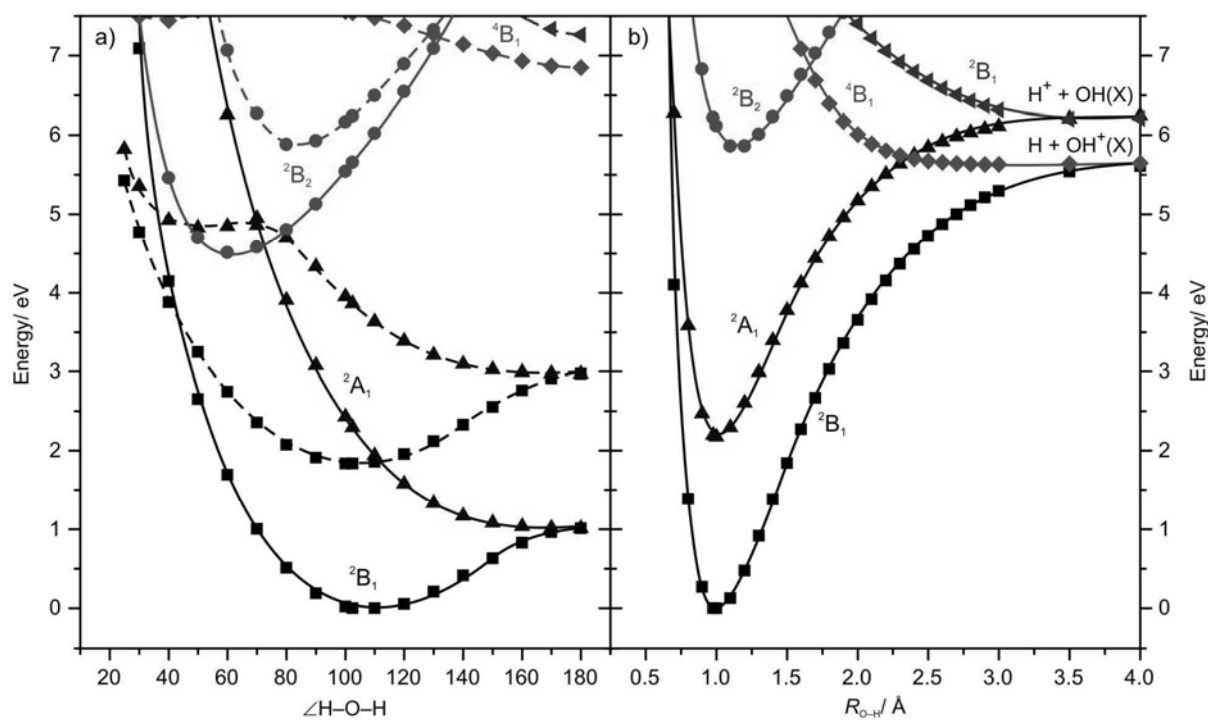


Figure 3



review Only

Figure 4

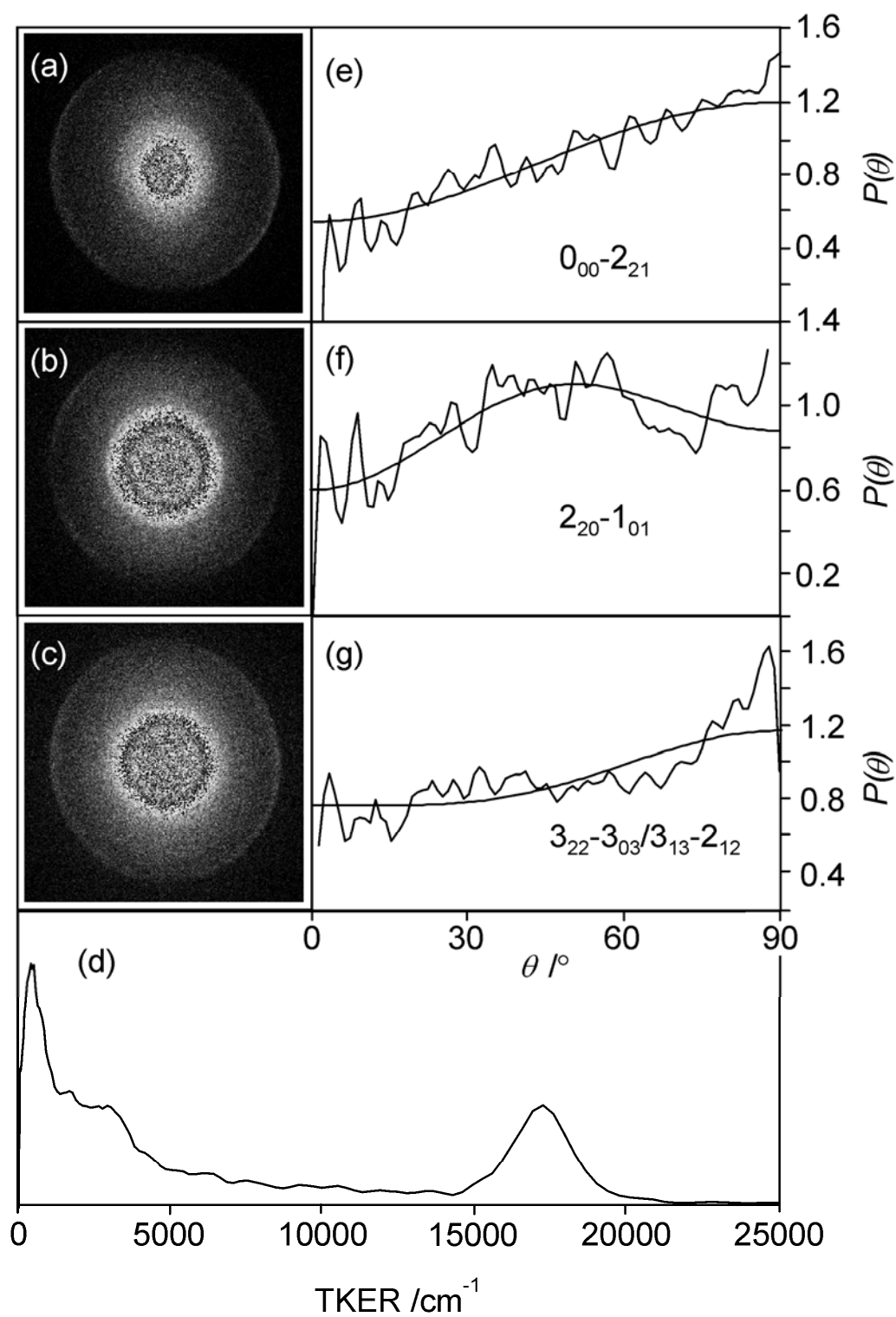
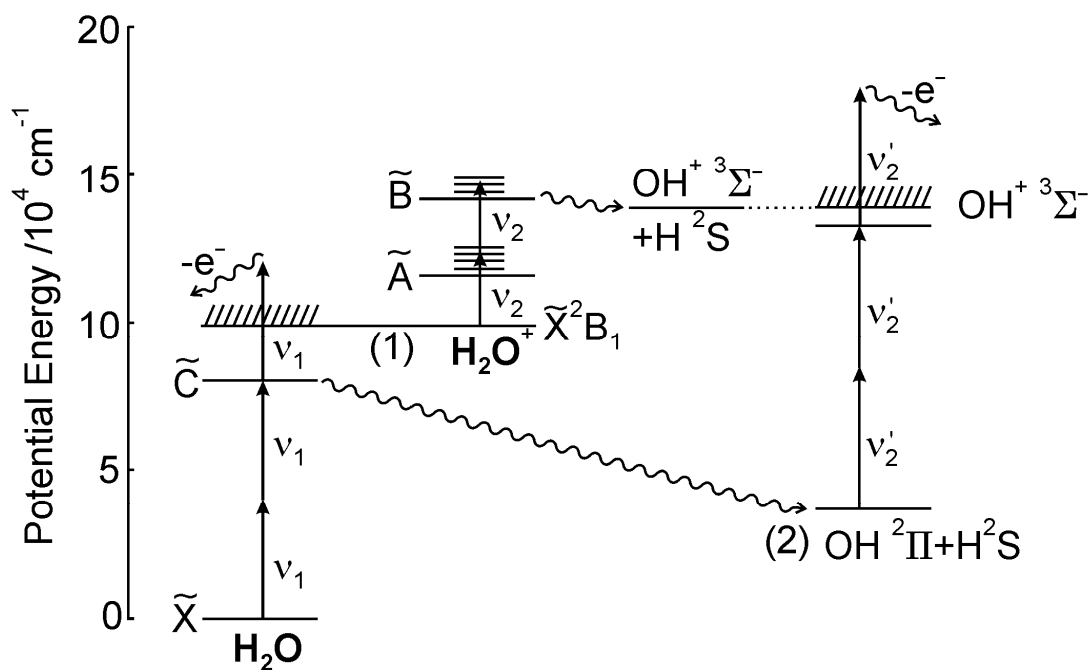


Figure 5



References

- 1 F. Aguirre and S.T. Pratt, *J. Chem. Phys.* **119**, 9476 (2003).
- 2 O.P.J. Vieuxmaire, M.G.D. Nix, J.A.J. Fitzpatrick, M. Beckert, R.N. Dixon and M.N.R. Ashfold, *Phys. Chem. Chem. Phys.* **6**, 543 (2004).
- 3 N.H. Nahler, O.P.J. Vieuxmaire, J.R. Jones, M.N.R. Ashfold, A.T.J.B. Eppink, A.M. Coriou and D.H. Parker, *J. Phys. Chem. A* **108**, 8077 (2004).
- 4 O.P.J. Vieuxmaire, N.H. Nahler, J.R. Jones, R.N. Dixon and M.N.R. Ashfold, *Mol. Phys.* **103**, 2437 (2005).
- 5 C.S. Chang, C.Y. Luo and K.P. Liu, *J. Phys. Chem. A* **109**, 1022 (2005).
- 6 M.H. Kim, B.D. Leskiw and A.G. Suits, *J. Phys. Chem. A* **109**, 7839 (2005).
- 7 A.D. Webb, N.H. Nahler, R.N. Dixon and M.N.R. Ashfold, *J. Chem. Phys.* **125**, 204312 (2006).
- 8 O.P.J. Vieuxmaire, N.H. Nahler, R.N. Dixon and M.N.R. Ashfold, *Phys. Chem. Chem. Phys.* **9**, 5531 (2007).
- 9 S.K. Lee, R. Silva, M.H. Kim, L. Shen and A.G. Suits, *J. Phys. Chem. A* **111**, 6741 (2007).
- 10 M.H. Kim, B.D. Leskiw, L. Shen and A.G. Suits, *J. Phys. Chem. A* **111**, 7472 (2007).
- 11 A.D. Webb, R.N. Dixon and M.N.R. Ashfold, *J. Chem. Phys.* **127**, 224307 (2007).
- 12 A.D. Webb, N. Kawanaka, R.N. Dixon and M.N.R. Ashfold, *J. Chem. Phys.* **127**, 224308 (2007).
- 13 M.H. Kim, L. Shen, H. Tao, T.J. Martinez and A.G. Suits, *Science* **315**, 1561 (2007).
- 14 A.D. Webb, N.H. Nahler and M.N.R. Ashfold, *J. Phys. Chem. A* **113**, 3773 (2009).
- 15 L. Shen, P.C. Singh, M.H. Kim, B.L. Zhang and A.G. Suits, *J. Phys. Chem. A* **113**, 68 (2009).
- 16 A.T.J.B. Eppink and D.H. Parker, *Rev. Sci. Instrum.* **68**, 3477 (1997).
- 17 M.N.R. Ashfold, N.H. Nahler, A.J. Orr-Ewing, O.P.J. Vieuxmaire, R.L. Toomes, T.N. Kitsopoulos, I. Anton-Garcia, D. Chestakov, S.-M. Wu and D.H. Parker, *Phys. Chem. Chem. Phys.* **8**, 26 (2006).
- 18 O. Dutuit, A. Tabache-Fouhaile, I. Nenner, H. Frohlich and P.M. Guyon, *J. Chem. Phys.* **83**, 584 (1985).
- 19 M.N.R. Ashfold and S.R. Langford, in *Rydberg States in Spectroscopy and Photochemistry*, (ed. C. Sandorfy), Kluwer Academic, Dordrecht (1999), pp. 23-56, and references therein.
- 20 X. Yang, *Int. Rev. Phys. Chem.* **24**, 37 (2005) and references therein.
- 21 G. Herzberg, *Ann. Geophys.* **36**, 605 (1980).
- 22 B.L.Lutz, M. Womak and R.M. Wagner, *Astrophys. J.*, **407**, 402 (1993).

- 1
2
3
4²³ D. Smith, *Chem. Rev.* **92**, 1473 (1992).
- 5
6²⁴ J. Leclerc, J.A. Horsley and J.C. Lorquet, *Chem. Phys.* **4**, 337 (1974).
- 7
8²⁵ R.N. Dixon, G. Duxbury, J.W. Rabalais and L. Asbrink, *Mol. Phys.* **31**, 423 (1976).
- 9
10²⁶ M. Brommer, B. Weis, B. Follmeg, P. Rosmus, S. Carter, N.C. Handy, H.J. Werner and P.J.
11 Knowles, *J. Chem. Phys.* **98**, 5222 (1993).
- 12
13²⁷ C.R. Brundle and D.W. Turner, *Proc. Roy. Soc. (Lond). A* **307**, 27 (1968).
- 14
15²⁸ L. Karlsson, L. Mattsson, R. Jadrny, R.G. Albridge, S. Pinchas, T. Bergmark and K.
16 Siegbahn, *J. Chem. Phys.* **62**, 4745 (1975).
- 17
18²⁹ J.E. Reutt, L.S. Wang, Y.T. Lee and D.A. Shirley, *J. Chem. Phys.* **85**, 6925 (1986).
- 19
20³⁰ S.Y. Truong, A.J. Yencha, A.M. Juarez, S.J. Cavanagh, P. Bolognesi and G.C. King, *Chem.*
21 *Phys.* **355**, 183 (2009) and references therein.
- 22
23³¹ F. Fiquet-Fayard and P.M. Guyon, *Mol. Phys.* **11**, 17 (1966).
- 24
25³² A.J. Lorquet and J.C. Lorquet, *Chem. Phys.* **4**, 353 (1974).
- 26
27³³ E. von Puttkamer, *Z. Naturforsch, Teil A* **35**, 1062 (1970).
- 28
29³⁴ J.H.D. Eland, *Chem. Phys.* **11**, 41 (1975).
- 30
31³⁵ I. Powis and D.J. Reynolds, *J. Chem. Soc. Faraday Trans.* **87**, 921 (1991).
- 32
33³⁶ D. Deharang, X. Chapisat, J.C. Lorquet, C. Galloy and G. Raseev, *J. Chem. Phys.* **78**, 1246
34 (1983).
- 35
36³⁷ M.N.R. Ashfold, J.M. Bayley and R.N. Dixon, *Chem. Phys.* **84**, 35 (1984).
- 37
38³⁸ M.N.R. Ashfold, J.M. Bayley and R.N. Dixon, *Can. J. Phys.* **62**, 1806 (1984).
- 39
40³⁹ G. Meijer, J.J. ter Meulen, P. Andresen and A. Bath, *J. Chem. Phys.* **85**, 6914 (1986).
- 41
42⁴⁰ W.L. Glab, M.S. Child and S.T. Pratt, *J. Chem. Phys.* **109**, 3062 (1998).
- 43
44⁴¹ B.W. Uselman, J.M. Boyle and S.L. Anderson, *Chem. Phys. Lett.* **440**, 171 (2007).
- 45
46⁴² See, for example, B. Das and J.W. Farley, *J. Chem. Phys.* **95**, 8809 (1991).
- 47
48⁴³ H. Lew, *Can. J. Phys.* **54**, 2028 (1976).
- 49
50⁴⁴ H. Lew and R. Groleau, *Can. J. Phys.* **65**, 739 (1987).
- 51
52⁴⁵ B. Ruscic, A.F. Wagner, L.B. Harding, R.L. Asher, D. Feller, D.A. Dixon, K.A. Peterson, Y.
53 Song, X.M. Qian, C.Y. Ng, J.B. Liu and W.W. Chen, *J. Phys. Chem. A* **106**, 2727 (2002).
- 54
55⁴⁶ R.G. Tonkyn, R. Wiedmann, E.R. Grant and M.G. White, *J. Chem. Phys.* **95**, 7033 (1991).
- 56
57⁴⁷ R.T. Wiedmann, R.G. Tonkyn and M.G. White, *J. Chem. Phys.* **97**, 768 (1992).
- 58
59⁴⁸ Yu. Ralchenko, A.E. Kramida J. Reader and [NIST ASD Team](#) (2008). *NIST Atomic Spectra*
60 *Database* (version 3.1.5), [Online]. Available: <http://physics.nist.gov/asd3> [2009, October 13].
National Institute of Standards and Technology, Gaithersburg, MD.

- 1
2
3
4 ⁴⁹ S.A. Harich, D.W.H. Hwang, J.J. Lin, X.M. Yang and R.N. Dixon, *J. Chem. Phys.* **113**, 10073
5
6 (2000).
7
8 ⁵⁰ E. Wrede, S. Laubach, S. Schulenburg, A. Brown, E.R. Wouters, A.J. Orr-Ewing and M.N.R.
9 Ashfold, *J. Chem. Phys.* **114**, 2629 (2001).
10
11 ⁵¹ Y. Sato, Y. Matsumi, M. Kawasaki, K. Tsukiyama and R. Bersohn, *J. Phys. Chem.* **99**, 16307
12
13 (1995).
14
15 ⁵² MOLPRO, version 2006.1, a package of *ab initio* programs; H.-J. Werner, P.J. Knowles, R.
16 Lindh, F.R. Manby, M. Schütz, P. Celani, T. Korona, G. Rauhut, R.D. Amos, A. Bernhardsson,
17 A. Berning, D.L. Cooper, M.J.O. Deegan, A.J. Dobbyn, F. Eckert, C. Hampel, G. Hetzer, A.W.
18 Lloyd, S.J. McNicholas, W. Meyer and M.E. Mura, A. Nicklass, P. Palmieri, R. Pitzer, U.
19 Schumann, H. Stoll, A.J. Stone, R. Tarroni and T. Thorsteinsson, Cardiff, 2006.
20
21 ⁵³ PGOPHER, a Program for Simulating Rotational Structure, C.M. Western, University of
22 Bristol, <http://pgopher.chm.bris.ac.uk>
23
24
25
26
27 ⁵⁴ W. Crofton, R.S. Altman, M.-F. Jagod and T. Oka, *J. Phys. Chem.* **89**, 3614 (1985).
28
29 ⁵⁵ T.R. Huet, C.J. Pursell, W.C. Ho, B.M. Dinelli and T. Oka, *J. Chem. Phys.* **97**, 5977 (1992).
30
31 ⁵⁶ F. Schneider, F. Di Giacomo and F.A. Gianturco, *J. Chem. Phys.* **105**, 7560 (1996).
32
33 ⁵⁷ K.-J. Yuan, Y. Cheng, L. Cheng, Q. Guo, D.-X. Dai, X.-Y. Wang, X.M. Yang and R.N.
34 Dixon, *Proc. Nat. Acad. Sci.* **105**, 19148 (2008).
35
36 ⁵⁸ E.R. Comben and J.M. Brown, *Chem. Phys.* **119**, 443 (1988).
37
38 ⁵⁹ D.H. Mordaunt, M.N.R. Ashfold and R.N. Dixon, *J. Chem. Phys.* **100**, 7360 (1994).
39
40 ⁶⁰ K-P. Huber and G. Herzberg, *Constants of Diatomic Molecules*, Van Nostrand Reinhold, New
41 York, London, 1979.
42
43 ⁶¹ M.E. Greenslade, M.I. Lester, D.Č. Radenović, A.J.A. van Rij and D.H. Parker, *J. Chem.*
44 *Phys.* **123**, 074309 (2005), and references therein.
45
46 ⁶² R.N. Dixon and T.W.R. Hancock, *J. Phys. Chem.* **101**, 7567 (1997).
47
48 ⁶³ R.N. Dixon, *J. Chem. Phys.* **122**, 194302 (2005).
49
50 ⁶⁴ M. Hochlaf, K.-M. Weitzel and C.Y. Ng, *J. Chem. Phys.* **120**, 6944 (2004).
51
52 ⁶⁵ J.H.D. Eland, *Int. J. Mass Spectrom. Ion Phys.* **31**, 161 (1979).
53
54 ⁶⁶ G. Hirsch and P.J. Bruna, *Int. J. Mass Spectrom. Ion Phys.* **36**, 37 (1980).
55
56 ⁶⁷ D.M. Hirst, *J. Chem. Phys.* **118**, 9175 (2003).
57
58 ⁶⁸ M.N.R. Ashfold, G.A. King, D. Murdock, M.G.D. Nix, T.A.A. Oliver and A.G. Sage,
59 accepted for publication in *Phys. Chem. Chem. Phys.*
60